This article has been accepted for publication in a future issue of this journal, but has not been fully edited. Content may change prior to final publication.
DOI: 10.17775/CSEEJPES.2024.02590

Multi-Damping Frequency-Constrained Unit Commitment and Multi-Reserve Resource Allocation for RES-Penetrated Power Systems

Chenyu Xu, *Student Member, IEEE,* Dongmei Zhao, Xiangyang Feng, Ran Tao, *and* Chongru Liu, *Senior Member, IEEE*

***Abstract*—The rapid influx of renewable energy sources (RESs) brings about significant impacts on the frequency dynamics and operational scheduling of power systems. RESs can provide rapid frequency support utilizing virtual inertia emulation or droop control. Nevertheless, the extensive integration of renewable energy generation amplifies the variability of crucial parameters in frequency control, leading to potential underdamped, overdamped, and critically damped states in the system frequency response model, thus affecting the performance of post-contingency frequency dynamics. To address this issue, this paper proposes a multi-damping state frequency response model. On the other hand, uncertainty surrounding renewable generation significantly impacts frequency security and system scheduling operations. This necessitates a more meticulous consideration of unit commitment (UC) and primary frequency reserves. To improve operational economics while stabilizing system frequency, the variable virtual inertia and droop factors of RESs are optimized for coordination with SGs. To this end, A robust frequency-constrained UC and multi-reserve resource allocation model is proposed. Simulation results validate the accuracy of the frequency response formula under multiple damping states, and comparative case studies demonstrate the effectiveness and scalability of the proposed model.**

***Index Terms*—Multi-damping states, variable virtual inertia and droop factors, frequency dynamics, unit commitment, reserve allocation**

NOMENCLATURE

Abbreviation

RESs	Renewable energy sources
SGs	Synchronous generators
IBRs	Inverter-based resources
UC	Unit commitment
PR	Frequency regulation
PFR	Primary frequency response
SFR	System frequency response

Indices and Sets

i	Index of SGs
j	Index of RESs
t	Index of time periods
s	Index of subspaces
n	Index of samples
Θ_s	Set of the subspace of definition domain Θ
$\mathbf{U}$	Set of uncertainty for RESs

Parameters

S_i^{sg}	Nominal capacity of SG i
S_j^{ibr}	Nominal capacity of RES j
f_0	Nominal frequency
$\dot{f}_{\max}$	RoCoF limit
$\Delta f_{\max}^{\lim}$	Frequency nadir limit
$\Delta f_{ss}^{\lim}$	Steady-state frequency deviation limit
ΔP_t	Power disturbance at time t
$\bar{M}_{ibr,j}$	Maximum virtual inertia of RES j
$\bar{D}_{ibr,j}$	Maximum droop factor of RES j
$c_{\mathrm{su},i}$ / $c_{\mathrm{sd},i}$	Start-up/ shut-down cost of SG i
$c_{on,i}$	The fixed cost of SG i
$c_{\mathrm{g},i}^{PR}$ / $c_{\mathrm{res},j}^{PR}$	PFR reserve cost coefficient of SG i/ RES j
$c_{\mathrm{g},i}^{\mathrm{up}}$ / $c_{\mathrm{g},i}^{\mathrm{down}}$	Upward/ downward reserve cost coefficient of SG i
$c_{\mathrm{pen},j}$	Penalty coefficient of power curtailment of RES j
$c_{\mathrm{re\text{-}disp},i}$	Re-scheduling power cost coefficient of SG i
$\rho_{i,l}$	Variable cost coefficient of SG i of the lth segment
$\bar{P}_i^{\mathrm{gen}}$ / $\underline{P}_i^{\mathrm{gen}}$	The upper/ lower limits of power generation of SG i
T_i^{on} / T_i^{off}	Minimum online/ offline time of SG i
$r_{\mathrm{u},i}$ / $r_{\mathrm{d},i}$	Upward/downward ramping limit of SG i
$r_{\mathrm{su},i}$ / $r_{\mathrm{sd},i}$	Maximum power generation at start-up/ shut-down of SG i
$P_{d,t}^{\mathrm{load}}$	Total system load
L_{SF}^{l}	Power transfer factor

This work was supported in part by the National Key R&D Program of China under Grant 2022YFB2402700, and in part by the Science and Technology Project of State Grid Corporation of China under Grant 52272222001J. (Corresponding author: Chenyu Xu).

Chenyu Xu, Dongmei Zhao, Xiangyang Feng, Chongru Liu are with the School of Electrical and Electronic Engineering, North China Electric Power University, Beijing 102206, China (e-mail: xu_chenyu2021@163.com).

Ran Tao is with State Grid Tianjin Electric Power Company, Hebei District, Tianjin 300010, China.

P_l^{cap}	Line capacity limit
$P_{j,t}^{av}$	Available power of RES *j* at time *t*
$\overline{P}_{j,t}^{MPPT}$ / $\underline{P}_{j,t}^{MPPT}$	Upper and lower bounds of fluctuation interval
Variables	
$z_{i,t}^{\text{SU}}$ / $z_{i,t}^{\text{SD}}$	Start-up/ shut-down action of SG *i* at time *t*
$u_{i,t}$	Binary variable indicating the on/off state of SG *i* at time *t*
$P_{i,t}^{\text{gen}}$	Generation power of SG *i* at time *t*
$p_{i,t,l}^{\text{gen}}$	Generation power of SG *i* at time *t* of the *l*th segment
$PR_{i,t}^{\text{gen}}$	PFR reserve capacities of SG *i* at time *t*
$R_{i,t}^{\text{gen}-}$ / $R_{i,t}^{\text{gen}+}$	Upward/ downward spinning reserve capacities of SG *i* at time *t*
$P_{j,t}^{\text{res}}$	Power output of RES *j* at time *t*
$PR_{j,t}^{\text{res}}$	PFR reserve capacities of RES *j* at time *t*
$z_{j,t}^{\text{u},+}$ / $z_{j,t}^{\text{u},-}$	Binary variable indicating upward/ downward fluctuation of RES *j* at time *t*
$P_{j,t}^{\text{MPPT,u}}$	Available Maximum generation power in the re-scheduling stage
$P_{i,t}^{\text{gen,u}}$ / $P_{j,t}^{\text{res,u}}$	Power output of SG *i*/ RES *j* at time *t* in the re-scheduling stage
$D_{ibr,j}$	Variable droop factor of RES *j*
$M_{ibr,j}$	Variable virtual inertia of RES *j*
M_{sys}^{t}	Synthetic inertia of the unified system at time *t*
D_{sys}^{t}	Synthetic damping of the unified system at time *t*

I. INTRODUCTION

THE modern power system is currently undergoing a significant transformation driven by the urgent need to achieve carbon-neutral objectives. Recent advancements in power electronics technology further propel this shift, facilitating the widespread integration of Inverter-based resources (IBRs) [1] [2]. However, Inverter-based RESs, such as solar photovoltaics (PVs) and wind turbines (WTs), are unable to provide inertia support and primary frequency response (PFR) under the traditional maximum power point tracking (MPPT) mode [3]. This development will decrease the system inertia level, thus escalating the risk of frequency instability [4].

Recent advancements in control technologies have delved into the potential of RESs to contribute to frequency support [5]. RESs endowed with appropriate control algorithms manifest inertia support and frequency response capability [6] [7]. Renewable generation is increasingly recognized as a crucial resource that can be coordinated with traditional SGs to provide frequency support.

Post-contingency frequency security has garnered increasing attention. On the one hand, allocating sufficient online SGs is a preventive instrument to mitigate rapid frequency variations. and keep the potential post-contingency frequency stable [8]. Great efforts have been made in previous works including considering frequency-constrained UC (FCUC) [9]-[12]. In [13], the proposed FCUC models further consider multi-area frequency security constraints in unit commitment, ensuring that each area has sufficient online SGs. Besides, some researchers have found that induction machines can provide inertial support like SGs [14] and have incorporated them into FCUC models. Based on this, the FCUC models in [15] comprehensively consider multi-area frequency response and the available inertia of induction machine loads. On the other hand, power systems require reserve certain capacities to compensate for power fluctuations. For SGs, they are required to reserve sufficient generation capacity [16]. The reserve capacity of SGs is mainly divided into two parts: non-contingency reserves and contingency reserves. Contingency reserves are aimed at addressing frequency security issues during high-power deficit events, with PFR reserves mainly emphasized. Non-contingency reserves are allocated to cope with the uncertainty associated with renewable generation. For RES units, they can operate in the de-loading mode providing up-reserve for PFR service. The generation power scheduling and the distribution of reserve capacities between SGs and RESs are closely intertwined. Their joint optimization can significantly improve the economic effectiveness and operational security during the UC phase. [17]. The extensive integration of RESs exacerbates interdependencies and strongly influences system frequency security. In light of this, the paper presents three pivotal questions that warrant further investigation.

i) Variability of frequency control parameters for RESs: Numerous studies have focused on integrating the FR capabilities of RESs into the frequency-constrained system operation issues. Zhang et al. analyzed the frequency support characteristics of wind farms and quantified their PFR reserve capacities [18]. In [19] [20], a frequency dynamics model that accounts for both the PR capabilities of SGs and the frequency support provided by RES stations is proposed and embedded into the UC stage. In these studies, the virtual inertia and droop factors of RESs were typically fixed. However, fixed control parameters have certain limitations, mainly manifested in the fact that the actual available renewable generation power may deviate from the day-ahead forecasted value due to the uncertainty of RESs. If the available generation falls short of the required PFR reserve, the PFR capacity from RESs will be constrained, leading to larger frequency deviations. Given that the majority of RESs can adapt their droop factors and virtual inertia in frequency control according to the security criteria of the power system, the frequency regulation of RESs demonstrates a level of flexibility [21]. Furthermore, Variable frequency control parameters also help better coordinate SGs and RESs to provide frequency support and enhance operational economics [22]. To this end, this paper proposes a novel approach where these parameters are treated as decision variables, and their values are optimized in the UC stage.

ii) Applicability of frequency dynamics model: Considerable effort has been devoted to establishing dynamic models following frequency disturbances. One approach is simulation-based [23] [24], which offers high precision but is challenging to apply in optimization models. For frequency-constrained optimization issues, two widely used mathematical methods exist: i) linear ramping model: [25]-[26] assume a linear relationship between output power and time during a primary frequency response period. However, this method decouples output power from frequency, failing to meet actual control requirements. ii) system frequency response (SFR) model [27]: This is another method for establishing dynamic frequency response models [19]. Indeed, the post-contingency frequency dynamics are influenced by all resources participating in primary frequency regulation. The extensive integration of RESs amplifies the variation ranges of crucial parameters in the SFR model, affecting the performance of post-contingency frequency dynamics. The damping ratio of the frequency dynamic response is expected to change, leading to potential underdamped, overdamped, and critically damped states in the system frequency response model [28]. Previous frequency dynamic studies based on the SFR model evidently overlook potential multiple damping modes while deriving the analytical time-domain frequency response, which may result in frequency deviation shifts and increase the risk of frequency insecurity. This paper incorporates the frequency support of RESs into the frequency dynamic model, deriving analytical expressions that reflect multiple damping states in frequency trajectories.

iii) Uncertainty of RES generation: The uncertainty of RES generation strongly impacts PFR reserve capacities and system scheduling operations. To cope with uncertainty, various optimization techniques for handling uncertainty have been proposed in previous literature, including scenario-probability approach [29] [30], chance-constrained stochastic approach [22] [31], robust optimization and its variant forms [16] [32]. It is necessary to associate uncertainty research with the FR capabilities of SGs and RESs for frequency security risk considerations.

In conclusion, given the complex coupling between the frequency dynamic characteristic, different frequency regulation resources, and the uncertainty associated with renewable generation, addressing frequency-constrained UC and multi-reserve resource optimization remains highly challenging. This is the focal point of this study. The main contributions of this paper can be outlined as follows:

1) Compared with the existing works in [2] [17] [18], A time-domain formulation for the SFR model adaptable to multi-damping states is proposed, which can accurately reflect frequency dynamics. Further, a linearization representation method has been introduced for frequency nadir.
2) SGs and RESs are coordinated to provide frequency support. For RES units, the variable virtual inertia and droop factors treated as decision variables, and their values are optimized in the UC stage to adaptively provide the PFC service and enhance operational economics.
3) A robust frequency-constrained UC and multi-reserve resource optimization model is proposed. Uncertainty in RES generation strongly impacts PFR capacities and system scheduling operations. This paper links uncertainty studies with the risks of frequency insecurity. Through extensive case studies, the effectiveness and scalability of the proposed model are demonstrated.

The remainder of the paper is organized as follows. Section II presents the frequency response model of hybrid SGs and IBRs in power systems and derives time-domain formulation for the frequency response model adaptable to multi-damping states. The models of robust frequency-constrained UC and reserve optimization model are formulated in Section III. Section IV presents the numerical experiments, and section V concludes this paper.

II. Frequency Dynamic Modeling of Hybrid SGs and IBRs in Power Systems

A. Modeling of Frequency Dynamics

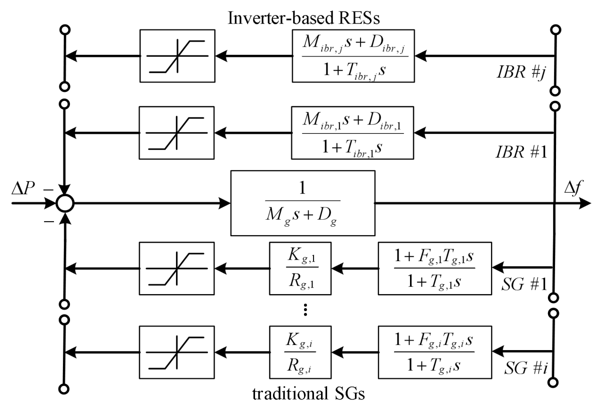

Fig. 1. Uniform frequency response model of hybrid SGs and IBRs in power systems

To portray the dynamics of system frequency in a tractable manner, Figure 1 depicts a simplified yet sufficiently accurate uniform frequency response model, comprising SGs and multiple IBRs. This model, based on mild assumptions as detailed in [33], employs the center of inertia (COI) concept. By amalgamating numerous SGs and IBRs into a single machine, it computes an average frequency while disregarding local frequency variations. In contrast to traditional SGs, the time constants of IBRs, denoted as T_{ibr} , are measured in milliseconds, approximately 2–3 orders of magnitude lower than those of SGs. Consequently, the time delay in frequency regulation of IBRs can be deemed negligible ($T_{ibr} \approx 0$).

The closed-loop transfer function of the frequency response model including SGs and IBRs can be expressed as follows:

$$G(s)=\frac{\Delta f(s)}{\Delta P(s)}=\Bigg\{\underbrace{(sM_g+D_g)+\sum_{i\in\Omega^S}\frac{K_{g,i}(1+sF_{g,i}T_{g,i})}{R_{g,i}(1+sT_{g,i})}}_{SGs}+\underbrace{\sum_{j\in\Omega^C}\frac{sM_{ibr,j}+D_{ibr,j}}{1+sT_{ibr,j}}}_{VSM-based\ \text{IBRs}}\Bigg\}^{-1} \tag{1}$$

Assuming that the time constants of SGs are similar, Eq. (1) can be represented as a second-order equation through parameter equivalence, as shown in (2).

$$G(s)=\frac{1}{MT}\frac{1+sT}{s^2+2\zeta\omega_n s+\omega_n^2} \tag{2}$$

Where:

$$\begin{cases} w_n=\sqrt{\dfrac{D+R}{MT}} \\ \zeta=\dfrac{M+T(D+F)}{2\sqrt{MT(D+R)}} \end{cases} \tag{3}$$

The equivalent parameters are listed below: [34]

$$\begin{cases} M=\dfrac{\sum_i M_{g,i}S_i^{sg}+\sum_j M_{ibr,j}S_j^{ibr}}{\sum_i S_i^{sg}+\sum_j S_j^{ibr}} \\ D=\dfrac{\sum_i D_{g,i}S_i^{sg}+\sum_j D_{ibr,j}S_j^{ibr}}{\sum_i S_i^{sg}+\sum_j S_j^{ibr}} \\ R=\dfrac{\sum_i K_{g,i}S_i^{sg}/R_{g,i}}{\sum_i S_i^{sg}+\sum_j S_j^{ibr}} \\ F=\dfrac{\sum_i K_{g,i}F_{g,i}S_i^{sg}/R_{g,i}}{\sum_i S_i^{sg}+\sum_j S_j^{ibr}} \end{cases} \tag{4}$$

Where $M_{g,i}$, $D_{g,i}$, $K_{g,i}$, $R_{g,i}$, $F_{g,i}$ denote the inertia constant, damping factor, power gain factor, speed regulation factor, and power fraction of SG i, respectively. $M_{ibr,j}$ and $D_{ibr,j}$ are the virtual inertia and droop factor of RES j.

Assuming a stepwise disturbance in active power denoted as $\Delta P(s)=\Delta P/s$, the analytical frequency response in the s-domain is presented in (5).

$$\Delta f(s)=\frac{\Delta P}{MT}\frac{1+sT}{s(s^2+2\zeta\omega_n s+\omega_n^2)} \tag{5}$$

The widespread introduction of IBRs has gradually altered the damping states in the frequency response model. The flexible adjustability of control parameters for IBRs enables the system to exhibit a multi-damping form. The discriminant Λ for determining whether the two-order dynamic system is underdamped or overdamped is shown in (6). Where ζ denotes the damping ratio in frequency response.

According to the value of Λ or ζ, the system may have three kinds of frequency regulation modes: underdamped ($\Lambda<0$ or $0<\zeta<1$), critical damped ($\Lambda=0$ or $\zeta=1$), and overdamped ($\Lambda>0$ or $\zeta>1$) responses.

$$\Lambda=\left(2\zeta\omega_n\right)^2-4\omega_n^2 \tag{6}$$

The characteristic roots of Eq.(5) vary in different damping states. Specifically, Eq. (5) has two complex roots in the underdamped state, while there are two distinct real roots in the overdamped state. In the critically damped state, there are two identical real roots. This leads to differences in the time-domain frequency response equations.

1) Underdamped Response

After applying an inverse Laplace transform on (5), we derive the analytical time-domain frequency response for the underdamped state as follows.

$$\begin{aligned}\Delta f(t)=\frac{\Delta P}{MT\omega_n^2}\{1+\frac{T\omega_n^2}{\omega_d}e^{-\omega_n\zeta t}[\sin\left(\omega_n\sqrt{1-\zeta^2}t\right)\\ -\frac{1}{\omega_n T}\sin\left(\omega_n\sqrt{1-\zeta^2}t+\phi\right)]\}\end{aligned} \tag{7}$$

Where $\phi=\sin^{-1}(\sqrt{1-\zeta^2})$ and $\omega_d=\sqrt{1-\zeta^2}\omega_n$.

Note that the time-domain formulation (7) derived for the *underdamped state* is consistent with the majority of literature such as [2] [17] [18].

2) Overdamped Response

The underdamped frequency response is solved as follows.

$$\begin{aligned}\Delta f(t)=\frac{\Delta P}{MT\omega_n^2}\{1-e^{-\omega_n\xi t}[\frac{1}{2}(1+\frac{\zeta-T\omega_n}{\sqrt{\zeta^2-1}})e^{w_n\sqrt{\zeta^2-1}t}\\ +\frac{1}{2}(1-\frac{\zeta-T\omega_n}{\sqrt{\zeta^2-1}})e^{-w_n\sqrt{\zeta^2-1}t}]\}\end{aligned} \tag{8}$$

If a trigonometric transformation is performed on (7), Eq. (7) can be rewritten as follows. (For the detailed derivation, see the Appendix)

$$\begin{aligned}\Delta f(t)=\frac{\Delta P}{MT\omega_n^2}\{1-e^{-\omega_n\xi t}[\cos\left(\omega_n\sqrt{1-\zeta^2}t\right)\\ +\frac{\zeta-T\omega_n}{\sqrt{1-\zeta^2}}\times\sin\left(\omega_n\sqrt{1-\zeta^2}t\right)]\}\end{aligned} \tag{9}$$

It can be observed that there are similar terms in (8) and (9). In this paper, the Euler formula $\cosh it=\cos t$, $\sinh it=i\sin t$, $\cosh t=(e^t+e^{-t})/2$, $\sinh t=(e^t-e^{-t})/2$ are introduced, and the overdamped formula (9) and the underdamped formula (8) can be unified as:

$$\Delta f(t)=\frac{\Delta P}{MT\omega_n^2}\left(1-\kappa_1 e^{\omega_1 t}-\kappa_2 e^{\omega_2 t}\right) \tag{10}$$

Where:

$$\begin{cases} \omega_1=\left(\sqrt{\zeta^2-1}-\zeta\right)\omega_n \\ \omega_2=\left(-\sqrt{\zeta^2-1}-\zeta\right)\omega_n \\ \kappa_1=\dfrac{\sqrt{\zeta^2-1}+\zeta-T\omega_n}{2\sqrt{\zeta^2-1}} \\ \kappa_2=\dfrac{\sqrt{\zeta^2-1}-\zeta+T\omega_n}{2\sqrt{\zeta^2-1}} \end{cases} \tag{11}$$

3) Critical Damped Response

The critical damped frequency response can be expressed as follows.

$$\Delta f(t)=\frac{\Delta P}{MT\omega_n^2}\left[1-e^{-\omega_n t}+(T\omega_n^2-\omega_n)te^{-\omega_n t}\right] \tag{12}$$

Overall, the frequency dynamics in multi-damping states is formulated by Eq.(13).

$$\Delta f(t)=\begin{cases}\dfrac{\Delta P}{MT\omega_n^2}\left(1-\kappa_1 e^{\omega_1 t}-\kappa_2 e^{\omega_2 t}\right),\zeta\neq 1\\ \dfrac{\Delta P}{MT\omega_n^2}\left[1-e^{-\omega_n t}+(T\omega_n^2-\omega_n)te^{-\omega_n t}\right],\zeta=1\end{cases} \tag{13}$$

B. Dynamic Metrics in Power Systems

The Fig. 2 illustrates the dynamic process of frequency response after a disturbance. Three frequency security metrics are introduced: the rate of change of frequency (RoCoF), the frequency nadir, and the steady-state frequency deviation, which are denoted by $\dot{f}$, Δf_{nadir}, and Δf_{ss}, respectively.

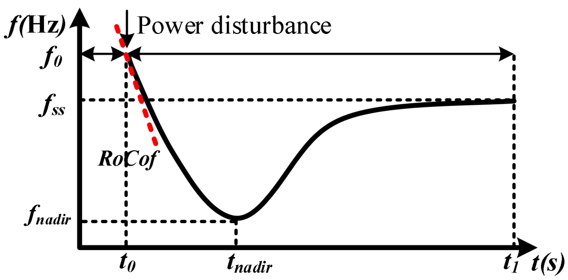

Fig. 2. Frequency dynamics process after a disturbance.

1) The Maximal RoCoF

In the initial seconds following a power disturbance, only inertia mitigates the frequency drop. Regardless of the damping state, the maximum RoCoF occurs at $t = t_0^+$ by taking the derivative of Eq.(13). To prevent triggering RoCoF relays, the RoCoF within the measurement window should be constrained.

$$\dot{f}=\frac{\Delta P}{MT\omega_n^2}\left(\kappa_1\omega_1+\kappa_2\omega_2\right)=\frac{\Delta P}{M} \tag{14}$$

2) The Steady-State Deviation

Primary frequency control action suppresses frequency decay and subsequently restores it to the steady state. The formula of steady-state frequency is unified given in (15), which is derived from (13) for $t \to \infty$.

$$\Delta f_{\rm ss}=\frac{\Delta P}{MT\omega_n^2}=\frac{\Delta P}{R+D} \tag{15}$$

3) The Frequency Nadir

Throughout the entire dynamic process, the frequency initially decreases before rising again, reaching a nadir with a deviation Δf_{nadir} at t_{nadir}. The timing of the frequency nadir is determined by identifying the moment at which the derivative of Eq.(13) equals zero.

$$\Delta f_{\rm nadir}=\begin{cases}\dfrac{\Delta P}{MT\omega_n^2}\left(1-\kappa_1 e^{\omega_1 t_{nadir}}-\kappa_2 e^{\omega_2 t_{nadir}}\right),\zeta\neq 1\\ \dfrac{\Delta P}{MT\omega_n^2}\left[1-e^{-\omega_n t'_{nadir}}+(T\omega_n^2-\omega_n)t'_{nadir}e^{-\omega_n t'_{nadir}}\right],\zeta=1\end{cases} \tag{16}$$

Where $t_{nadir}=\dfrac{\ln(-\kappa_1\omega_1/\kappa_2\omega_2)}{\omega_2-\omega_1}$, $t'_{nadir}=T/(T\omega_n-1)$ denote the time instance of frequency nadir corresponding to different damping states.

The post-contingency frequency security requires above frequency security metrics within their thresholds.

$$\left|\Delta\dot{f}\right|\le \dot{f}_{\max} \tag{17}$$

$$\left|\Delta f_{\rm ss}\right|\le \Delta f_{\rm ss}^{\rm lim} \tag{18}$$

$$\left|\Delta f_{\rm nadir}\right|\le \Delta f_{\max}^{\rm lim} \tag{19}$$

C. Linearization Methodology for Frequency Nadir

The expression of frequency nadir in (16) is nonlinear to variables M, D, R, F. The Δf_{nadir} can be presented in compact form as follows:

$$\Delta f_{\rm nadir}=\Delta P\cdot \mathrm{F}\ (M,D,R,F) \tag{20}$$

The piecewise linearization technique [28] is employed to approximate the feasible region of the function $\Phi(M, D, R, F)$ and the detailed process of resolving unfolds as follows:

Step 1: The Monte Carlo sampling method was performed over the upper and lower limits of system inertia M, damping factor D, droop gain R, and power fraction F to obtain initial data samples, ensuring that sufficient samples were available for simulating each damping state. Then, calculate the value of function $\Phi(\cdot)$ corresponding to each sample.

Step 2: The nonlinear function $\Phi(\cdot)$ is approximated by several hyperplanes. Assuming the domain of the function $\Phi(\cdot)$ is defined as $\Theta = \{(M, D, R, F)\}$, the fundamental concept of piecewise linearization is to partition this domain into a series of subspaces, denoted as Θ_s $(s = 1, 2, ..., S)$. S denotes the number of subspaces. In each subspace, the nonlinear function $\Phi(\cdot)$ is approximated by the hyperplane H_s. The linear equations of hyperplane H_s are as follows:

$$\mathrm{H}_s(M,D,R,F)\,|_{(M,D,R,F)\in\Theta_s}=\kappa_s^M M+\kappa_s^D D+\kappa_s^R R+\kappa_s^F F+\kappa_s^C \tag{21}$$

Where $\kappa_s^M, \kappa_s^D, \kappa_s^R, \kappa_s^F, \kappa_s^C$ are the combining parameters that determine the hyperplane in subspace Θ_s.

Step 3: The following model is utilized to determine the value of κ for each hyperplane.

$$\min_{\kappa}\sum_{s=1}^{S}\sum_{n=1}^{N_s}[\mathrm{H}_{n,s}-\mathrm{F}\ (M_{n,s},D_{n,s},R_{n,s},F_{n,s})]^2 \tag{22}$$

$$\text{s.t.}\ (M_{n,s},D_{n,s},R_{n,s},F_{n,s})\in\Theta_s,\forall n \tag{23}$$

$$\mathrm{F}\ (M_{n,s},D_{n,s},R_{n,s},F_{n,s})\le \mathrm{H}_s,\forall n,s \tag{24}$$

Where $\kappa=\left\{(\kappa_s^M,\kappa_s^D,\kappa_s^R,\kappa_s^F,\kappa_s^C)\right\}_{s=1}^{S}$ are the coefficients that determine the hyperplanes. n and N_s denote the index and the number of samples in subspace Θ_s. Constraint (24) is aimed at preventing an insecure case from being misidentified as a secure case, ensuring frequency robustness.

III. Mathematical Formulation of Robust Frequency-Constrained UC And Multi-Reserve Resource Optimization Model

In this section, a robust frequency-constrained UC and multi-reserve resource optimization model is proposed. The upper-level model is a deterministic model based on frequency constraints, aimed at optimizing the UC decisions of SGs, frequency regulation parameters (i.e., the virtual inertia and droop factors) of RESs, and power scheduling and reserve allocation between SGs and RESs. The lower-level model adapts output power based on the uncertainty of renewable generation.

A. The Overall Model

Objective (25) in the upper level is to minimize total operational cost of SGs and RESs. The max-min function (50) in the lower level aims to reduce the re-scheduling cost of SGs and the penalty cost for wind power curtailment.

Upper level:

$$\min\left\{\begin{array}{l}\sum_{t,i}(c_{\mathrm{su},i}z^{\mathrm{SU}}_{i,t}+c_{\mathrm{sd},i}z^{\mathrm{SD}}_{i,t}+\Gamma^{\mathrm{gen}}_{i,t})+\sum_{t,j}c^{PR}_{\mathrm{res},j}PR^{\mathrm{res}}_{j,t}\\ +\sum_{t,i}(c^{PR}_{\mathrm{g},i}PR^{\mathrm{gen}}_{i,t}+c^{\mathrm{up}}_{\mathrm{g},i}R^{\mathrm{gen+}}_{i,t}+c^{\mathrm{down}}_{\mathrm{g},i}R^{\mathrm{gen-}}_{i,t})\end{array}\right\} \tag{25}$$

$$\begin{cases}\Gamma^{\mathrm{gen}}_{i,t}=c_{on,i}u_{i,t}+\sum_{l}\rho_{i,l}p^{\mathrm{gen}}_{i,t,l}\\ P^{\mathrm{gen}}_{i,t}=\underline{P}^{\mathrm{gen}}_{i}u_{i,t}+\sum_{l}p^{\mathrm{gen}}_{i,t,l}\\ 0\le p^{\mathrm{gen}}_{i,t,l}\le(\overline{P}^{\mathrm{gen}}_{i}-\underline{P}^{\mathrm{gen}}_{i})/N_{pw}\end{cases} \tag{26}$$

$$z^{\mathrm{SU}}_{i,t}+z^{\mathrm{SD}}_{i,t}\le 1,\ \forall i,t \tag{27}$$

$$u_{i,t+1}=u_{i,t}+z^{\mathrm{SU}}_{i,t}-z^{\mathrm{SD}}_{i,t},\ \forall i,t \tag{28}$$

$$-u_{i,t-1}+u_{i,t}\le u_{i,\tau},\ \forall i,t\le\tau\le T^{\mathrm{on}}_{i}+t-1 \tag{29}$$

$$u_{i,t-1}-u_{i,t}+u_{i,\tau}\le 1,\ \forall i,t\le\tau\le T^{\mathrm{off}}_{i}+t-1 \tag{30}$$

$$P^{\mathrm{gen}}_{i,t+1}-P^{\mathrm{gen}}_{i,t}\le u_{i,t}r_{\mathrm{u},i}+(1-u_{i,t})r_{\mathrm{su},i}\ ,\forall i,t \tag{31}$$

$$P^{\mathrm{gen}}_{i,t-1}-P^{\mathrm{gen}}_{i,t}\le u_{i,t}r_{\mathrm{d},i}+(1-u_{i,t})r_{\mathrm{sd},i}\ ,\forall i,t \tag{32}$$

$$\underline{P}^{\mathrm{gen}}_{i}u_{i,t}\le P^{\mathrm{gen}}_{i,t}\le\overline{P}^{\mathrm{gen}}_{i}u_{i,t}\ ,\forall i,t \tag{33}$$

$$PR^{\mathrm{gen}}_{i,t}\ge u_{i,t}\frac{1}{R_{sg,i}}S^{sg}_{i}\frac{\Delta f^{lim}_{ss}}{f_0}\ ,\forall i,t \tag{34}$$

$$\underline{P}^{\mathrm{gen}}_{i}u_{i,t}\le P^{\mathrm{gen}}_{i,t}+PR^{\mathrm{gen}}_{i,t}+R^{\mathrm{gen+}}_{i,t}\le\overline{P}^{\mathrm{gen}}_{i}u_{i,t}\ ,\forall i,t \tag{35}$$

$$\underline{P}^{\mathrm{gen}}_{i}u_{i,t}\le P^{\mathrm{gen}}_{i,t}+PR^{\mathrm{gen}}_{i,t}-R^{\mathrm{gen-}}_{i,t}\le\overline{P}^{\mathrm{gen}}_{i}u_{i,t}\ ,\forall i,t \tag{36}$$

$$R^{\mathrm{gen+}}_{i,t}\ge 0,R^{\mathrm{gen-}}_{i,t}\ge 0\ ,\forall i,t \tag{37}$$

$$0\le P^{\mathrm{res}}_{j,t}\le P^{av}_{j,t}\ ,\forall j,t \tag{38}$$

$$PR^{\mathrm{res}}_{j,t}\ge D_{ibr,j}S^{ibr}_{j}\frac{\Delta f^{lim}_{max}}{f_0}+M_{ibr,j}S^{ibr}_{j}\frac{\dot{f}^{lim}}{f_0}\ ,\forall j,t \tag{39}$$

$$0\le P^{\mathrm{res}}_{j,t}+PR^{\mathrm{res}}_{j,t}\le P^{av}_{j,t}\ ,\forall j,t \tag{40}$$

$$\sum_{i}P^{\mathrm{gen}}_{i,t}+\sum_{j}P^{\mathrm{res}}_{j,t}=\sum_{d}P^{\mathrm{load}}_{d,t},\ \forall t \tag{41}$$

$$\left|\sum_{i}L^{l}_{\mathrm{SF},i}P^{\mathrm{gen}}_{i,t}+\sum_{j}L^{l}_{\mathrm{SF},j}P^{\mathrm{res}}_{j,t}-\sum_{d}L^{l}_{\mathrm{SF},d}P^{\mathrm{load}}_{d,t}\right|\le P^{\mathrm{cap}}_{l}\ ,\forall l,t \tag{42}$$

Frequency constraints:

$$M^{t}_{sys}=\frac{\left(\sum_{i}u_{i,t}M_{g,i}S^{sg}_{i}+\sum_{j}M_{ibr,j,t}S^{ibr}_{j}\right)}{\sum_{i}S^{sg}_{i}+\sum_{j}S^{ibr}_{j}} \tag{43}$$

$$D^{t}_{sys}=\frac{\left(\sum_{i}u_{i,t}D_{g,i}S^{sg}_{i}+\sum_{j}D_{ibr,j,t}S^{ibr}_{j}\right)}{\sum_{i}S^{sg}_{i}+\sum_{j}S^{ibr}_{j}} \tag{44}$$

$$0\le M_{ibr,j,t}\le\overline{M}_{ibr,j},\ \forall j,t \tag{45}$$

$$0\le D_{ibr,j,t}\le\overline{D}_{ibr,j},\ \forall j,t \tag{46}$$

$$M^{t}_{sys}\ge\frac{f_0\Delta P_t}{\dot{f}_{\max}} \tag{47}$$

$$D^{t}_{sys}\ge\frac{f_0\Delta P_t}{\Delta f^{lim}_{ss}}-\frac{1}{\sum_{i}S^{sg}_{i}+\sum_{j}S^{ibr}_{j}}\sum_{i}\frac{u_{i,t}K_{sg,i}S^{sg}_{i}}{R_{sg,i}} \tag{48}$$

$$f_0\Delta P_t\cdot\left(\mathrm{H}_{s}(M^{t}_{sys},D^{t}_{sys},R^{t}_{sys},F^{t}_{sys})\big|_{(M^{t}_{sys},D^{t}_{sys},R^{t}_{sys},F^{t}_{sys})\in\Theta_s}\right)\le\Delta f^{lim}_{\max} \tag{49}$$

Regarding the SGs, Constraint (26) formulates the fuel cost Γ^{gen} of the SGs, defining it as a piecewise linear function dependent on the generation power P^{gen}. N_{pw} is the number of piecewise segments. Constraints (27) - (28) represent the logical relationship between the operation status and the shut-down / start-up actions of SGs. Constraints (29)-(30) delineate the minimum online and offline durations for SGs. Constraints (31) - (32) describe the ramp-up/down restrictions of SGs. Constraint (33) describes the generation capacities of SGs. In this paper, the reserve capacity of SGs is mainly divided into two parts: non-contingency reserves and contingency reserves. Contingency reserves are aimed at addressing frequency security issues during high-power deficit events, with primary frequency response reserves mainly emphasized. To provide primary frequency regulation, SGs should keep adequate reserves as shown in (34) . Non-contingency reserves are intended to address the uncertainty of renewable generation, Constraints (35)-(37) ensure sufficient upward and downward reserves of SGs.

As for the RES units, Constraint (38) describes the adjustable range of power output of RESs. Constraint (39) ensures that the virtual inertia and droop control power does not exceed the PFR reserve of RES units. Constraint (40) restricts the power output of RES unit less than its available power $P^{av}_{j,t}$.

Constraint (41) ensures the system power balance. Constraints (42) describe the line capacity limits. Constraints (43)-(49) are formulated for system frequency security after a disturbance. In particular, (43) and (44) calculate the overall inertia and damping of the power systems. Constraints (45)-(46) restrict the upper limits of frequency control parameters of RES units for the technical capabilities and physical constraints. Eq. (47)-(48) reflect the constraints of RoCoF and steady-state frequency deviation. In (47) , the constraint of RoCoF can be formulated by a linear constraint on M^{t}_{sys}. In (48) , the steady-state frequency constraint is a linear expression with respect to D^{t}_{sys}. Constraint (49) describes the frequency nadir constraints, utilizing the linearization model in II-C.

Lower level:

$$\max_{z\in\mathbf{U}}\min_{x^{\mathrm{u}}\in\mathbf{\Omega}^{\mathrm{u}}}\sum\nolimits_{t,j}c_{\mathrm{pen},j}(P_{j,t}^{\mathrm{MPPT,u}}-P_{j,t}^{\mathrm{res,u}}-PR_{j,t}^{\mathrm{res}}) +\sum\nolimits_{t,i}c_{\text{re-disp},i}\left|P_{i,t}^{\mathrm{gen,u}}-P_{i,t}^{\mathrm{gen}}\right| \tag{50}$$

$$-R_{i,t}^{\mathrm{gen-}}\le P_{i,t}^{\mathrm{gen,u}}-P_{i,t}^{\mathrm{gen}}\le R_{i,t}^{\mathrm{gen+}},\forall i,t \tag{51}$$

$$\underline{P}_i^{\mathrm{gen}}u_{i,t}\le P_{i,t}^{\mathrm{gen,u}}\le \overline{P}_i^{\mathrm{gen}}u_{i,t},\forall i,t \tag{52}$$

$$P_{i,t+1}^{\mathrm{gen,u}}-P_{i,t}^{\mathrm{gen,u}}\le u_{i,t}r_{\mathrm{u},i}+(1-u_{i,t})r_{\mathrm{su},i}\ ,\forall i,t \tag{53}$$

$$P_{i,t-1}^{\mathrm{gen,u}}-P_{i,t}^{\mathrm{gen,u}}\le u_{i,t}r_{\mathrm{d},i}+(1-u_{i,t})r_{\mathrm{sd},i}\ ,\forall i,t \tag{54}$$

$$0\le P_{j,t}^{\mathrm{res,u}}\le P_{j,t}^{\mathrm{MPPT,u}}\ ,\forall j,t \tag{55}$$

$$0\le P_{j,t}^{\mathrm{res,u}}+PR_{j,t}^{\mathrm{res}}\le P_{j,t}^{\mathrm{MPPT,u}}\ ,\forall j,t \tag{56}$$

$$\sum\nolimits_i P_{i,t}^{\mathrm{gen,u}}+\sum\nolimits_j P_{j,t}^{\mathrm{res,u}}=\sum\nolimits_d P_{d,t}^{\mathrm{load}},\ \forall t \tag{57}$$

$$\left|\sum\nolimits_i L_{\mathrm{SF},i}^l P_{i,t}^{\mathrm{gen,u}}+\sum\nolimits_j L_{\mathrm{SF},j}^l P_{j,t}^{\mathrm{res,u}}-\sum\nolimits_d L_{\mathrm{SF},d}^l P_{d,t}^{\mathrm{load}}\right|\le P_l^{\mathrm{cap}},\forall l,t \tag{58}$$

Constraint (51) ensures the re-scheduling power less than the non-contingency reserves of SGs. (52)-(56) are the re-scheduling constraints of SGs and RESs. Besides, the power balance constraint (57) and line capacity limit constraint (58) should be considered in the re-scheduling period.

B. Uncertainty Description

The renewable generation uncertainty could be modeled as the following box uncertainty set [35]:

$$\mathbf{P}^{\mathbf{MPPT,u}}=\{P_{j,t}^{\mathrm{MPPT,u}}\ \big|\ P_{j,t}^{\mathrm{MPPT,u}}=P_{j,t}^{av}+z_{j,t}^{\mathrm{u},+}P_{j,t}^{h}-z_{j,t}^{\mathrm{u},-}P_{j,t}^{\mathrm{h}}\} \tag{59}$$

$$\mathbf{U}=\left\{\begin{array}{l} z_{j,t}^{\mathrm{u},+}+z_{j,t}^{\mathrm{u},-}\le 1,\forall j,\forall t, z_{j,t}^{\mathrm{u},+},z_{j,t}^{\mathrm{u},-}\in\{0,1\}\\ \sum\nolimits_t (z_{j,t}^{\mathrm{u},+}+z_{j,t}^{\mathrm{u},-})\le\Gamma_j^{\mathrm{T}},\ \forall j\\ \sum\nolimits_j (z_{j,t}^{\mathrm{u},+}+z_{j,t}^{\mathrm{u},-})\le\Gamma_t^{\mathrm{S}},\ \forall t \end{array}\right\} \tag{60}$$

Where $P_{j,t}^{\mathrm{h}}=(\overline{P}_{j,t}^{MPPT}-\underline{P}_{j,t}^{MPPT})/2$. $P_{j,t}^{h}$ denotes the uncertainty margin of RESs.

C. A Two-Stage Robust Optimization Framework

1) Dealing with the Absolute Operators in the Object: $|\cdot|$ operator is expressed in a general form as follows:

$$\min|y|\Leftrightarrow\left\{\begin{array}{c}\min t\\ s.t.\ \ t\ge y,\ t\ge -y\end{array}\right. \tag{61}$$

2) Solution Based on C&CG Algorithm [36]*:* The proposed min-max-min robust optimization model can be presented in compact form as:

$$\begin{gathered}\min_{x^0\in\mathbf{\Omega}^0}(\mathbf{c_x^0})^{\mathrm{T}}\boldsymbol{x^0}+\max_{z\in\mathbf{U}}[(\mathbf{c_w^u})^{\mathrm{T}}\mathbf{P}^{\mathbf{MPPT,u}}+\min_{x^{\mathrm{u}}\in\mathbf{\Omega}^{\mathrm{u}}}(\mathbf{c_x^u})^{\mathrm{T}}\boldsymbol{x^u}]\\ \mathbf{\Omega}^0=\{\boldsymbol{x}^0|\boldsymbol{E}\boldsymbol{x}^0\le\boldsymbol{e},\ \boldsymbol{F}\boldsymbol{x}^0=\boldsymbol{f}\}\\ \mathbf{\Omega}^{\mathrm{u}}=\{\boldsymbol{x}^{\mathrm{u}}|\boldsymbol{G}\boldsymbol{x}^{\mathrm{u}}\le\boldsymbol{H}\boldsymbol{x}^0+\boldsymbol{I}\boldsymbol{z}+\boldsymbol{J},\boldsymbol{M}\boldsymbol{x}^{\mathbf{u}}=\boldsymbol{m}\}\\ U=\{z\,|\,\boldsymbol{W}\boldsymbol{z}\le\boldsymbol{w}\}\end{gathered} \tag{62}$$

Where $\boldsymbol{x^0}$ and $\boldsymbol{x^u}$ denote the model optimization variables in the first and second stages, respectively; $\boldsymbol{z}$ is the variable in the uncertainty set; $\mathbf{P}^{\mathbf{MPPT,u}}$ denotes the uncertainty variables. $\mathbf{c_x^0}$, $\mathbf{c_w^u}$, $\mathbf{c_x^u}$, $\boldsymbol{E}$, $\boldsymbol{e}$, $\boldsymbol{F}$, $\boldsymbol{f}$, $\boldsymbol{G}$, $\boldsymbol{H}$, $\boldsymbol{I}$, $\boldsymbol{J}$, $\boldsymbol{M}$, $\boldsymbol{m}$, $\boldsymbol{W}$, $\boldsymbol{w}$ are constant coefficient vectors or matrices.

i) Master Problem (MP): Initializing the main problem and Adding constraints to the main problem:

$$\begin{gathered}\min_{x^0\in\mathbf{\Omega}^0}(\mathbf{c_x^0})^{\mathrm{T}}\boldsymbol{x^0}+\eta\\ s.t.\left\{\begin{array}{l}\boldsymbol{E}\boldsymbol{x}^0\le\boldsymbol{e},\ \boldsymbol{F}\boldsymbol{x}^0=\boldsymbol{f}\\ \eta\ge(\mathbf{c_w^u})^{\mathrm{T}}\mathbf{P}_k^{\mathbf{MPPT,u}}+(\mathbf{c_x^u})^{\mathrm{T}}\boldsymbol{x}_k^{\mathbf{u}},\ \forall 0\le k\le i-1\\ \boldsymbol{G}\boldsymbol{x}_k^{\mathbf{u}}\le\boldsymbol{H}\boldsymbol{x}^0+\boldsymbol{I}\boldsymbol{z}_k^*+\boldsymbol{J},\boldsymbol{M}\boldsymbol{x}_k^{\mathbf{u}}=\boldsymbol{m},\ \forall 0\le k\le i-1\end{array}\right.\end{gathered} \tag{63}$$

Where η is the objective function of the SP to be optimized; $\boldsymbol{z}_k^*$ characterizes the worst-case uncertainty found by the SP in the k^{th} iteration.

The optimal solution is denoted as $\boldsymbol{x}_{(i)}^{0*}$ by solving the MP (63). Update the lower bound by $LB=\max(LB,\eta^{(i)})$.

ii) Sub-Problem (SP): Solving the feasibility-check sub-problem:

$$\begin{gathered}f_{\mathrm{sp}}:=\max_{z\in\mathbf{U}}[(\mathbf{c_w^u})^{\mathrm{T}}\mathbf{P}^{\mathbf{MPPT,u}}+\max_{z\in\mathbf{U}}\min_{x^{\mathrm{u}}\in\mathbf{\Omega}^{\mathrm{u}}}(\mathbf{c_x^u})^{\mathrm{T}}\boldsymbol{x^u}]\\ s.t.\left\{\begin{array}{l}\mathbf{\Omega}^{\mathrm{u}}=\{\boldsymbol{x}^{\mathrm{u}}|\boldsymbol{G}\boldsymbol{x}^{\mathrm{u}}\le\boldsymbol{H}\boldsymbol{x}_{(i)}^{0*}+\boldsymbol{I}\boldsymbol{z}+\boldsymbol{J},\boldsymbol{M}\boldsymbol{x}^{\mathrm{u}}=\boldsymbol{m}\}\\ \boldsymbol{U}=\{z\,|\,\boldsymbol{W}\boldsymbol{z}\le\boldsymbol{w}\}\end{array}\right.\end{gathered} \tag{64}$$

The max-min model of SP can be converted into a single-level equivalent model through strong duality theory [37], and solved directly using commercial solvers. The SP during the i iteration can be expressed in (65).

$$\begin{gathered}\max(\mathbf{c_w^u})^{\mathrm{T}}\mathbf{P}^{\mathbf{MPPT,u}}+(\boldsymbol{H}\boldsymbol{x}_{(i)}^{0*}+\boldsymbol{I}\boldsymbol{z}+\boldsymbol{J})^{\mathrm{T}}\boldsymbol{\xi}+\boldsymbol{m}^{\mathrm{T}}\delta\\ s.t.\left\{\begin{array}{l}\boldsymbol{G}^{\mathrm{T}}\boldsymbol{\xi}+\boldsymbol{M}^{\mathrm{T}}\delta\le\mathbf{c_x^u}\\ \boldsymbol{\xi}\le 0,\ \delta\ \text{unlimied}\\ \boldsymbol{W}\boldsymbol{z}\le\boldsymbol{w}\end{array}\right.\end{gathered} \tag{65}$$

The bilinear term $\boldsymbol{z}^{\mathrm{T}}\boldsymbol{\xi}$ consists of the multiplication of continuous variables and binary variables, which can be rigorously transformed by the big-M method [38]. Solve the SP (65). Then, update the upper bound by $UB=\min(UB,f_{\mathrm{sp}}^{(i)})$.

iii) Termination Check: If $|(UB-LB)/UB|\le\varepsilon$, the algorithm terminates and outputs the optimal solution; otherwise, update i=i+1, then proceed to Step 2. Here, ε represents the iteration threshold.

IV. Case Study

In this study, the accuracy of the frequency response formulation under multi-damping states is validated. Subsequently, we analyze the impacts of frequency security constraints, uncertainty, and the benefits of adopting flexible virtual inertia and droop factors, utilizing a modified PJM 5-bus system. Finally, the scalability of the approach is demonstrated using the IEEE 118-bus system.

A. Multi-Damping Frequency Dynamics

1) The Effectiveness of the Multi-Damping Frequency Dynamics: A 100 MW power imbalance (approximately 5% of the rated capacity) is set. 7 sets of experiments were conducted to test the frequency dynamics in different damping states by adjusting the virtual inertia and damping factor of the wind farms. Out of these, three sets were underdamped, one was critically damped, and three were overdamped. In addition, a frequency response model based on Simulink simulation is established to analyze the frequency dynamics to contrast with the proposed multi-damping frequency response formulation.

The comparison graphs between Simulink simulation results and those derived from multi-damping SFR are shown in Fig. 3. The numerical values of the frequency nadir and errors are presented in Table I. The results reveal a high consistency between the multi-damping state formulation and the actual simulation. This is mainly due to the lower time constants of power electronic inverters compared to those of synchronous generators, which can be neglected. Thus, it validates the correctness of the multi-damping state frequency response formulation proposed in this paper.

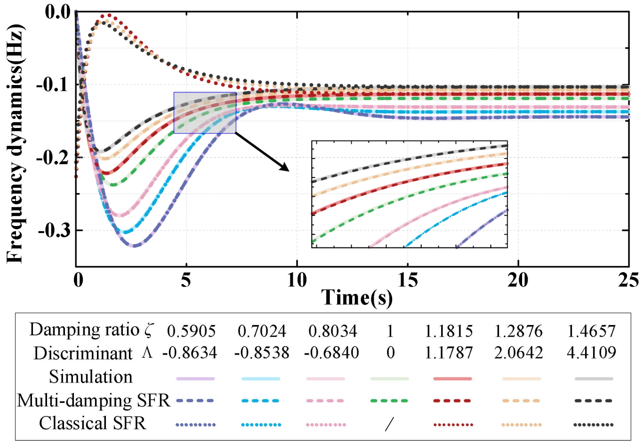

Fig. 3. Frequency dynamics in different damping ratios using the simulation-based method, multi-damping state formulation, and classical SFR model.

TABLE I
ERROR COMPARISON IN DIFFERENT DAMPING STATES

Damping state	Simulink simulation	Multi-damping SFR	Err.	Classical SFR	Err.
ζ=0.5905 (Λ=-0.8634)	-0.3208	-0.3214	0	-0.3214	0
ζ=0.7024 (Λ=-0.8538)	-0.3022	-0.3029	0	-0.3029	0
ζ=0.8034 (Λ=-0.6840)	-0.2797	-0.2802	0	-0.2802	0
ζ=1 (Λ=0)	-0.2377	-0.2377	0	-	-
ζ=1.1815 (Λ=1.1787)	0.2220	-0.2217	0	-0.0045	97.97%
ζ=1.2876 (Λ=2.0642)	-0.2020	-0.2016	0	-0.0130	93.56%
ζ=1.4657 (Λ=4.4109)	-0.1921	-0.1915	0	-0.0151	92.14%

2) Comparison with Existing Methods: A comparative analysis is conducted between the method proposed in this paper and the classical SFR model adopted in [39].

The frequency dynamics and frequency nadir metric are reported in Fig. 3 and Table I, respectively. The above results indicate that the classical SFR model cannot provide a reasonable estimate of the frequency dynamics. In the overdamped state, the frequency dynamics exhibited a trend opposite to the actual behavior, failing to reflect the true frequency dynamics. The classical SFR expression involves quadrant division and the application of auxiliary angle formulas [39]. If the underdamped frequency response equation is forcibly applied in the overdamped state, it will result in significant deviations in frequency dynamics from the actual values. And this will also result in a non-zero frequency deviation at t=0$^+$.

The introduction of the Euler formula in this study circumvented the judgment of underdamped and overdamped states, effectively unifying them into a single equation. Additionally, the critical damping state was covered, rendering the frequency response model more comprehensive and adaptable to a wider range of operating conditions.

B. A Modified PJM 5-Bus Systems

The modified PJM-5 bus system is for analysis [40]. The system consists of 5 SGs and 2 WTs. The WTs are connected to buses A and D with respective capacities of 300 MW, as shown in Fig. 4. The main technical parameters of SGs are listed in Table II. Relative economic parameters and line parameters can be found in [32]. The virtual inertia and damping variable ranges for WTs are [0,10] p.u. and [0,15] p.u., respectively.

The uncertainty margin for RESs is set as 10% of the predicted value. The temporal robustness budgets are set as $\Gamma_1^{\mathrm{T}} = \Gamma_2^{\mathrm{T}} = 6$, and the spatial budget is set as $\Gamma_t^{\mathrm{S}} = 2, \forall t$. In each period, a power disturbance of 10% of the total load is considered [9]. The nominal system frequency is $f_0 = 50\mathrm{Hz}$, and the frequency security thresholds for this case are defined as $\Delta f_{\max}^{\lim} = 0.5\mathrm{Hz}, \Delta f_{ss}^{\lim} = 0.2\mathrm{Hz}, \dot{f}^{\lim} = 0.5\mathrm{Hz/s}$.

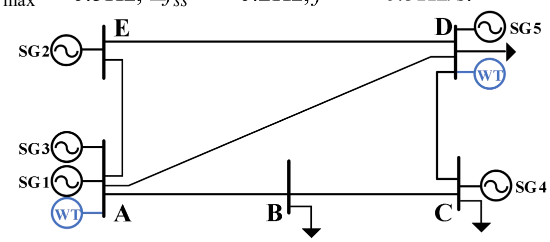

Fig. 4. Modified PJM 5-bus systems.

TABLE II
MAIN TECHNICAL PARAMETERS OF SYNCHRONOUS GENERATORS

Param.	SG1	SG2	SG3	SG4	SG5
Location	A	E	A	C	D
Capacity (MW)	70	570	100	520	200
Minimum output (MW)	40	170	40	100	50
Ramp rate (MW/h)	40	150	40	200	80
Min. on/off time(h)	3	8	5	8	6
Inertia constant (s)	4.2	6.6	5.2	6.7	5.2
Droop factor (p.u.)	12	17	13	17	14
Damping (p.u.)	1.5	2	1.8	2	1.8

To demonstrate the effectiveness of the method proposed in this article, several comparative cases were set up and analyzed.

1) The Impact of Frequency Security Constraints:

Case 1: a robust frequency-constrained UC and reserve optimization model (this paper).

Case 2: a traditional UC model without frequency constraints. And WTs run in the MPPT mode.

In Case 2, our focus is on disregarding frequency security constraints but requiring that the PFR reserve capacities of the SG exceed the power disturbance. Fig. 5 shows the metrics describing the post-contingency frequency dynamic performance in different periods. It is noticeable that the frequency metrics cannot remain within the threshold for all time intervals. During the whole period, the maximum RoCoF is 1.0059Hz/s, and the maximum frequency deviation and steady-state deviation are 0.8169Hz and 0.3670Hz, respectively, which exceeds the limit of the frequency security metrics.

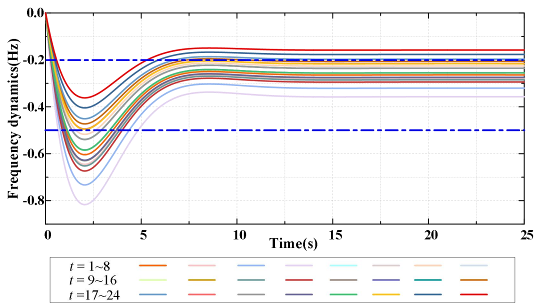

Fig. 5. The performance of frequency dynamics in Case 2.

In contrast, the improvement of frequency security is achieved at the expense of operation costs in Case 1. The optimal unit commitment and detailed operation results in Case 1 and Case 2 are depicted in Fig. 6 and Table III. Focusing on Case 1, the additional unit SG5 is started at t=6, which provides more inertia and PFR capacities compared to that in Case 2. However, it also increases the startup and shutdown cost of the unit. Secondly, SGs and RESs are coordinated to provide frequency support. To mitigate potential frequency instability issues, both SGs and WTs reserved additional primary frequency response reserves. As a result, the maximum RoCoF is 0.5000 Hz/s, and the maximum frequency deviation reaches 0.4471 Hz and 0.2000 Hz at the nadir and the steady state respectively, notably lower than those observed in Case 1.

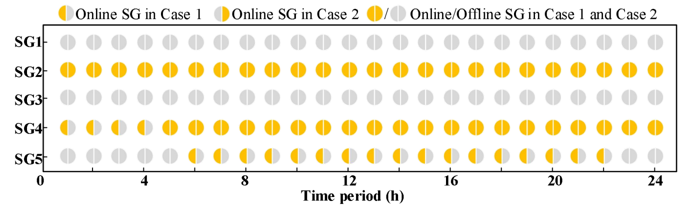

Fig. 6. Optimal unit commitment in Case 1 and Case 2.

The accuracy of linearization constraints for frequency nadir is evaluated by comparing the formulation results (F-Rs) derived from this paper with the linearization results (L-Rs). Fig. 7 depicts the post-contingency frequency nadir of these two methods in different periods. The performance details are in Table IV. The maximal relative error is 2.03%. The results show that the linearized results can accurately estimate the frequency nadir. Moreover, the absolute values of linearized results are greater than the simulation value, which does not overestimate the security of the frequency. The results are conservative, ensuring the original frequency nadir constraint remains feasible.

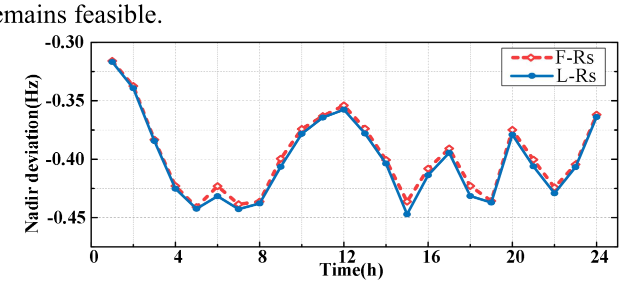

Fig. 7. Frequency nadir error.

TABLE III
OPERATION RESULTS IN CASE 1-4

Comparison terms		*Case 1*	*Case 2*	*Case 3*	*Case 4*
Economic cost	Start-up & shut-down cost ($)	1800	5000	3580	1800
	Fuel cost of SGs ($)	297707	272496	321076	297653
	PFR reserve cost of SGs ($)	16438	17898	16320	15556
	Non-contingency reserve cost of SGs ($)	5288	5328	5206	0
	PFR reserve cost of WTs ($)	3347	0	9360	4571
	Wind curtailment penalties ($)	4752	3902	5164	0
	Total cost ($)	329332	304624	360706	319580
Frequency metrics	Maximum $\dot{f}$ (Hz/s)	0.5000	1.0059	0.4736	0.5000
	Maximum Δf_{nadir} (Hz)	0.4471	0.8169	0.3793	0.4471
	Maximum Δf_{ss} (Hz)	0.2000	0.3670	0.1998	0.2000

TABLE IV
THE FREQUENCY NADIR DERIVED FROM FORMULATION AND LINEARIZATION TECHNOLOGY

Time slot t	F-Rs	L-Rs	Err.	Time slot t	F-Rs	LRs	Err.
1	0.3159	0.3167	0.26%	13	0.3738	0.3780	1.11%
2	0.3374	0.3392	0.55%	14	0.4006	0.4037	0.77%
3	0.3833	0.3843	0.26%	15	0.4363	0.4471	2.48%
4	0.4229	0.4252	0.56%	16	0.4081	0.4136	1.36%
5	0.4410	0.4424	0.32%	17	0.3908	0.3945	0.95%
6	0.4231	0.4317	2.03%	18	0.4229	0.4315	2.03%
7	0.4385	0.4427	0.96%	19	0.4357	0.4371	0.31%
8	0.4363	0.4378	0.35%	20	0.3749	0.3791	1.11%
9	0.3996	0.4065	1.72%	21	0.4004	0.4061	1.43%
10	0.3741	0.3783	1.10%	22	0.4241	0.4292	1.19%
11	0.3631	0.3643	0.34%	23	0.4045	0.4067	0.55%
12	0.3540	0.3576	1.03%	24	0.3619	0.3639	0.55%

* For ease of presentation, frequency metrics are expressed in absolute values.

2) Benefits of Adopting Variable Frequency Regulation Parameters: To evaluate the benefit of adopting feasible virtual inertia and droop factors of RESs, a third model is considered.

Case 3: WF1 with a fixed virtual inertia and droop factor at 6 p.u. and 6 p.u.. WF2 with a fixed virtual inertia and droop factor at 6 p.u. and 8 p.u..

From the perspective of frequency stability, compared to Case 1, Case 3 does not fully exploit the feasibility of utilizing renewable generation as flexible PR resources. Due to the insufficient frequency regulation capability of renewable generation, traditional synchronous generator units must be forcibly started up to provide inertia and reserve support for frequency stability during certain periods. Unit commitment results are shown in Fig. 8. Specifically, during the 10-14 period, G5 starts up at $t = 10$ due to a significant power deficit. G3 has already started up at time slot 8, constrained by the minimum operating duration of the unit. G1 starts up at time slot 12 until 14. During the evening peak periods of 19-21, SG1 starts up to maintain system frequency stability.

Fig. 9 depicts the variable inertia and droop factor of RESs at different time slots. As shown in Fig. 9, RES units can enhance frequency regulation capability during these periods by increasing virtual inertia and droop factors. In other periods, online units can address potential frequency security issues, thus renewable energy does not need to provide frequency support, maximizing generation to improve system economics.

From the perspective of operational economics, as shown in Table III, compared to fixed frequency control parameters, the startup and fuel costs of synchronous generators significantly increase in Case 3. Additionally, multiple generator startups lead to a higher level of wind resource curtailment to meet the requirements of unit minimum output. In contrast, in Case 1, there is an 8.70% reduction in total costs. These findings suggest that optimizing variable virtual inertia and droop factors can enhance the coordination of various frequency regulation resources, thereby improving operational economics.

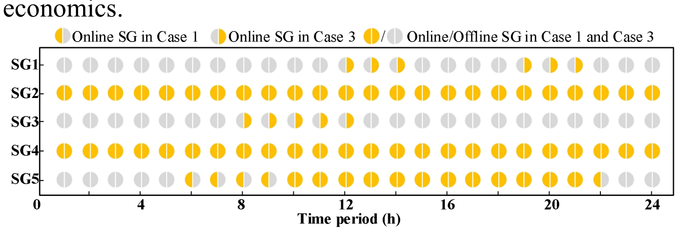

Fig. 8. Optimal unit commitment in Case 1 and Case 3.

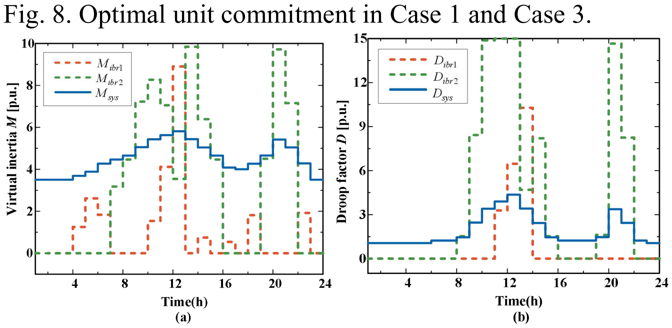

Fig. 9. Variable inertia and droop factor of RESs at different periods (a) virtual inertia; (b) droop factor.

Post-contingency frequency metrics in different cases are demonstrated in Fig. 10. As the frequency control parameters are fixed and the UC process is discrete, status change of a unit will significantly impact frequency trajectories, posing challenges in finding a UC solution that precisely satisfies all frequency security thresholds as shown in Case 3. On the contrary, the frequency parameters of RESs are flexible and continuously adjustable. In Case 1, it can be observed from Fig.10 the optimization results of M_{ibr} may lead to the RoCoF right hitting the boundary as RoCoF is linearly correlated with system inertia. Similarly, as steady-state frequency deviation is linearly correlated with system damping, the optimization results of D_{ibr} may result in instances where the steady-state frequency deviation precisely hits the boundary.

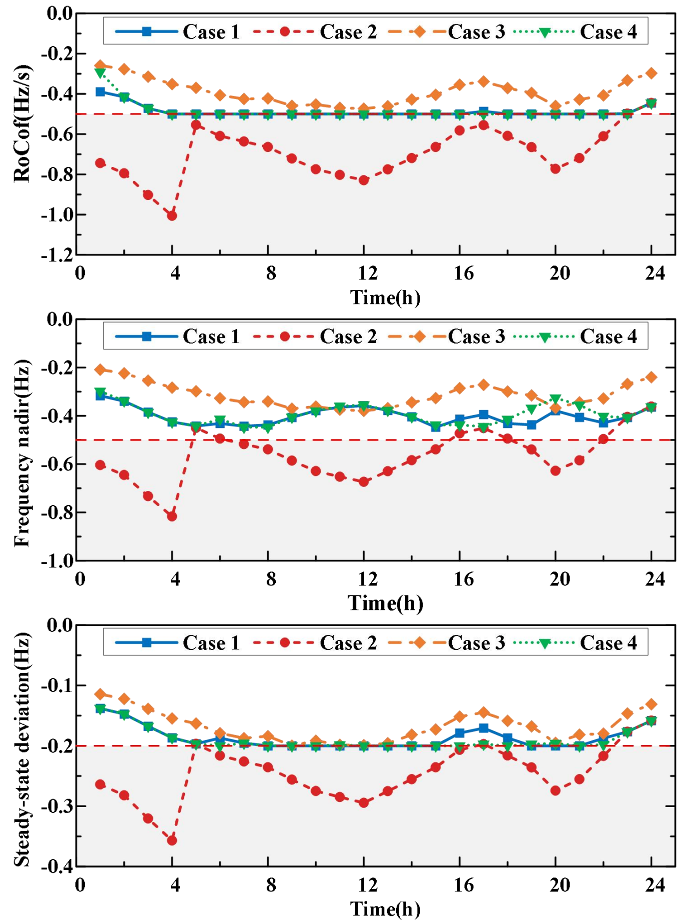

Fig. 10. Post-contingency frequency metrics: (a) maximum RoCoF, (b) frequency nadir, and (c) steady-state frequency deviation.

3) The Impact of Uncertainty: To evaluate the impact of the uncertainty of RESs, a fourth model is introduced.

Case 4: deterministic frequency-constrained approach.

The optimal UC solution for Case 4 is presented in Fig. 11, along with detailed performance metrics in Table III. The robust constrained approach explicitly takes the possibility that the available wind power is lower than predicted into account, thereby making a higher allocation of generation and non-contingency reserves on SGs. Thus, compared to Case 4, the cost of reserve cost increases by 24.57%, and the total cost increases by 3.05% in Case 1.

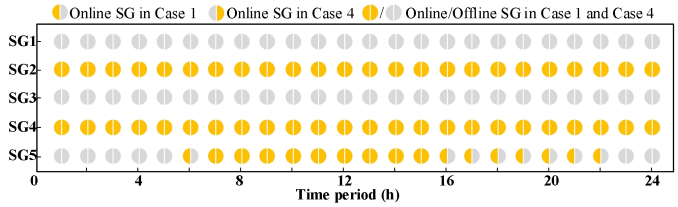

Fig. 11. Optimal unit commitment in Case 1 and Case 4.

Next, we vary the temporal robustness budgets to assess the impact on the total cost of the proposed model. The results are reported in Fig.12. As uncertainty increases from 0 to 12, a discernible trend emerges: the operating costs of the system steadily rise, indicating that decisions made by operators become more conservative. Therefore, striking a balance between operational economy and uncertainty risk is crucial.

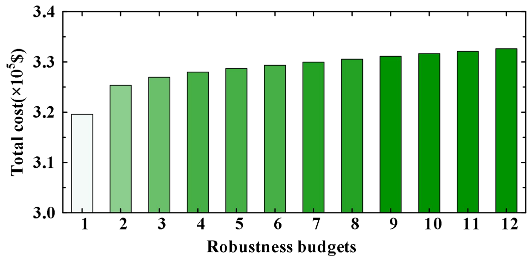

Fig. 12. Uncertainty analysis of system operation.

4) Necessity of Multi-Damping State Modeling: To further illustrate the necessity of multi-damping state modeling in the frequency-constrained UC and reserve allocation (FCUC-RA) model, a fifth model is constructed.

Case 5: Frequency security constraint modeling based on the classical SFR model in the deterministic FCUC-RA model.

Table V shows the frequency nadir metrics and damping ratios at each period. When t=12, 20, 21, the system is in overdamped states. The estimated values of frequency nadir adopting the classical SFR model are significantly lower than those obtained with the multi-damping SFR model, with errors of -11.74%, -18.86%, and -20.69%, respectively. It can be seen that the classical SFR model cannot reflect the frequency dynamics of overdamped states, resulting in the underestimation of the frequency nadir metric. Thus, the classical SFR model poses a risk of violating frequency security limits.

Furthermore, we use the existing control parameters at t = 21 and increase the system disturbance from the original 10% to 15%. The frequency nadir is estimated to be 0.2201 Hz utilizing the classical SFR-constrained FCUC-RA model, mistakenly believing that the frequency will not exceed the frequency security limit. However, the frequency nadir reaches 0.5304 Hz in reality, exceeding the limit. This indicates that the classical SFR method is more optimistic and cannot correctly assess the risk of system frequency.

As the scale and number of variable parameters of frequency regulation expand in the power systems, the damping in the frequency response model will change, leading to more complex frequency dynamics. It becomes difficult to estimate the system damping in advance before the unit commitment and reserve optimization stage. Therefore, designing a frequency nadir expression that is suitable for multi-damping states becomes extremely necessary. This work fills this gap.

C. Scalability Test

To further analyze the performance of the proposed model, The IEEE 118-bus system is utilized for scalability tests. The modified system consists of 54 SGs, 6 wind farms (WFs), and four photovoltaic plants (PVs). Six wind farms are connected to buses 1, 35, 44, 50, 82, 97 with 400 MW, 330 MW, 400 MW, 400 MW, 330 MW, 330 MW, and four photovoltaic plants to buses 20, 52, 47, 81 with installed capabilities of 400 MW, 200MW, 200 MW, 300 MW, respectively. The penetration rate of renewable generation is 31.30%. The relative parameters are from [41].

Fig. 13 shows the frequency performance during the whole period. In Case 2, the maximum RoCoF is 0.8294Hz/s the maximum frequency deviation is 0.6012Hz, and the maximum and steady-state deviation is 0.2451Hz. It is noticeable that the frequency metrics exceed the limit of the frequency security metrics. In contrast, they remain within the threshold for all time intervals in Case 1 from Fig. 13(a).

In Case 1, SGs and RESs are coordinated to provide frequency support. From the perspective of RES frequency regulation, the frequency control parameters exhibit a certain degree of flexibility at different periods. Fig. 14 illustrates the variable virtual inertia of RESs and overall inertia of the system, variable droop factor of RESs and overall damping of the system for 10 renewable energy stations, respectively. The results validate the need for RES to provide frequency support for power systems with high-RES penetration.

TABLE V

THE DAMPING RATIOS AND FREQUENCY NADIR METRICS FOR MULTI-DAMPING SFR AND CLASSICAL SFR MODEL

Time slot t	Damping ratio ζ	Multi-damping SFR (MD-SFR)	Classical SFR (C-SFR)	Err.	Time slot t	Damping ratio ζ	Multi-damping SFR (MD-SFR)	Classical SFR (C-SFR)	Err.
1	0.7090	0.3159	0.3163	0.03%	13	0.9054	0.3738	0.3917	1.78%
2	0.7090	0.3374	0.3380	0.06%	14	0.8148	0.4006	0.4093	0.87%
3	0.7090	0.3833	0.3843	0.10%	15	0.7102	0.4363	0.4378	0.15%
4	0.6974	0.4229	0.4237	0.08%	16	0.7268	0.4303	0.4329	0.26%
5	0.6859	0.4410	0.4421	0.11%	17	0.6855	0.4417	0.4431	0.14%
6	0.7857	0.4100	0.4124	0.25%	18	0.7849	0.4102	0.4126	0.23%
7	0.6885	0.4385	0.4411	0.25%	19	0.8925	0.3774	0.3806	0.31%
8	0.7102	0.4363	0.4378	0.15%	20	**1.0570**	**0.3359**	**0.1473**	**-18.86%**
9	0.8180	0.3996	0.4021	0.25%	21	**1.0278**	**0.3536**	**0.1467**	**-20.69%**
10	0.9043	0.3741	0.3834	0.93%	22	0.7896	0.4087	0.4131	0.44%
11	0.9452	0.3631	0.3794	1.63%	23	0.7090	0.4045	0.4055	0.11%
12	**1.0264**	**0.3540**	**0.2365**	**-11.74%**	24	0.7090	0.3619	0.3623	0.04%

* Err=(C-SFR − MD-SFR) / MD-SFR×100%.

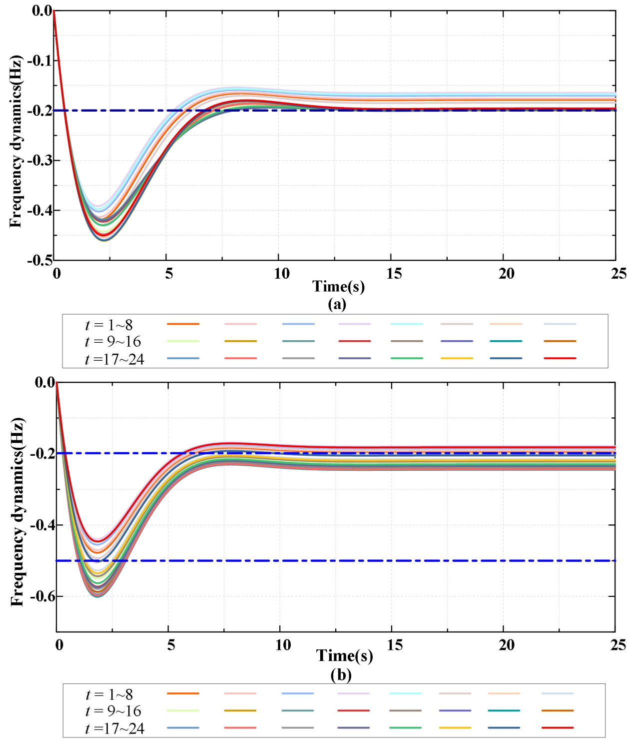

Fig. 13 The performance of frequency dynamics (a) in Case 1; (b) in Case 2.

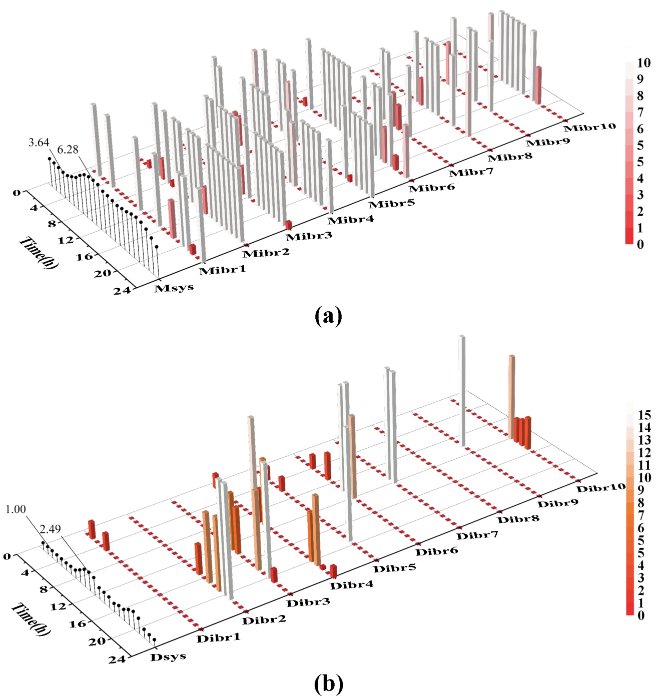

Fig. 14. Variable inertia and droop factor of RESs at different periods (a) virtual inertia of RESs and overall inertia of the system; (b) droop factor of RESs and overall damping of the system.

From Table VI, compared to Case 2, the PFR reserve cost of SGs decreases by 22.51% in Case 1, while the total reserve cost remains similar to Case 2. However, the overall system cost increases by 8.11% due to the additional unit.

In addition, the size of the scalability test and the time consumption are be reported. Specifically, the extended model initially handles 51793 continuous variables, 4368 binary variables, and 16941 constraints. After the presolve phase, there are finally 27025 continuous variables and 3982 binary variables in the branch and bound process. The computation time for solving the proposed model is 1219.53s.

Above results indicate the scalability and effectiveness of the robust optimal UC and multi-resource reserve optimization considering the frequency security proposed in this paper.

TABLE VI
OPERATION RESULTS IN CASE 1 AND CASE 2 FOR *IEEE 118-BUS SYSTEM*

Comparison terms	*Case 1*	*Case 2*
Start-up & shut-down cost ($)	2949	2080
Fuel cost of SGs ($)	1343214	1234184
PFR reserve cost of SGs ($)	76673	98942
Non-contingency reserve cost of SGs ($)	22601	24859
PFR reserve cost of WTs ($)	21665	0
Wind curtailment penalties ($)	14967	10802
Total cost ($)	1482069	1370867
Maximum $\dot{f}$ (Hz/s) (Hz/s)	0.5000	0.8294
Maximum Δf_{nadir} (Hz)	0.4669	0.6012
Maximum Δf_{ss} (Hz)	0.2000	0.2451

V. CONCLUSION

This paper proposes a UC and multi-reserve resource allocation model considering multi-damping states of frequency security constraints. In this model, the complex coupling among frequency dynamic characteristics, different frequency regulation resources, and uncertainties associated with renewable energy generation are considered. Numerical results indicate the following points:

1) The extensive integration of renewable energy generation amplifies the variability of crucial parameters in frequency control, leading to potential underdamped, overdamped, and critically damped states in the SFR model. This paper derives multi-damping frequency response formulation. Simulation results indicate consistency with the proposed method and exhibit high precision.

2) In highly penetrated power systems, relying solely on traditional SGs for frequency stability poses significant risks. Case studies confirm the necessity of RES units as frequency support units and the consideration of frequency stability constraints.

3) SGs and RESs are coordinated to provide frequency support. Leveraging variable virtual inertia and droop factors can greatly enhance the coordination among various frequency regulation resources, leading to cost reductions.

4) Uncertainty in RES generation strongly impacts PFR reserve capacities and system scheduling operations. To address this uncertainty, a robust UC and reserve allocation model is proposed, and C&CG algorithm is employed to solve the robust optimization problem.

5) The model presented in this paper is scalable and demonstrates good performance on the IEEE 118-bus system.

With the continuous development of control technologies, both grid-forming and grid-following control techniques have been explored, leading to differences in the contribution of RES to frequency support and thus affecting the performance of frequency dynamics. Future research should focus on this characteristic. Additionally, further attention is needed on the spatial characteristics of frequency distribution.

VI Appendix

The derivation from equation (7) to equation (9) is as follows.

The time-domain frequency response for the underdamped state can be represented by (66) (originally Eq.(7)).

$$\Delta f(t)=\frac{\Delta P}{MT\omega_n^2}\{1+\frac{T\omega_n^2}{\omega_d}e^{-\omega_n\zeta t}[\sin\left(\omega_n\sqrt{1-\zeta^2}t\right) -\frac{1}{\omega_n T}\sin\left(\omega_n\sqrt{1-\zeta^2}t+\phi\right)]\} \tag{66}$$

Where $\phi=\sin^{-1}(\sqrt{1-\zeta^2})$ and $\omega_d=\sqrt{1-\zeta^2}\omega_n$.

Substituting ω_d into Eq.(66) yields the following.

$$\Delta f(t)=\frac{\Delta P}{MT\omega_n^2}\{1+\frac{T\omega_n}{\sqrt{1-\zeta^2}}e^{-\omega_n\zeta t}[\sin\left(\omega_n\sqrt{1-\zeta^2}t\right) -\frac{1}{\omega_n T}\sin\left(\omega_n\sqrt{1-\zeta^2}t+\phi\right)]\} \tag{67}$$

From $\phi=\sin^{-1}(\sqrt{1-\zeta^2})$, we obtain $\sin\phi=\sqrt{1-\zeta^2}$ and $\cos\phi=\zeta$. Using trigonometric transformation formulas, Eq.(67) can be converted into:

$$\Delta f(t)=\frac{\Delta P}{MT\omega_n^2}\{1+\frac{T\omega_n}{\sqrt{1-\zeta^2}}e^{-\omega_n\zeta t}[\frac{\omega_n T-\zeta}{T\omega_n}\sin\left(\omega_n\sqrt{1-\zeta^2}t\right) -\frac{\sqrt{1-\zeta^2}}{T\omega_n}\cos\left(\omega_n\sqrt{1-\zeta^2}t\right)]\} \tag{68}$$

After further simplification, Eq.(68) can be expressed as:

$$\Delta f(t)=\frac{\Delta P}{MT\omega_n^2}\{1-e^{-\omega_n\zeta t}[\cos\left(\omega_n\sqrt{1-\zeta^2}t\right) +\frac{\zeta-\omega_n T}{\sqrt{1-\zeta^2}}\sin\left(\omega_n\sqrt{1-\zeta^2}t\right)]\} \tag{69}$$

Therefore, Eq.(66) is equivalent to Eq.(69).

References

[1] O. O. Khamisov, M. Ali, T. Sayfutdinov, Y. Jiang, V. Terzija, and P. Vorobev, "A Novel Contingency-Aware Primary Frequency Control for Power Grids with High CIG-Penetration," *IEEE Trans. Power Syst.*, pp. 1–14, 2023.

[2] B. She, F. Li, H. Cui, J. Wang, Q. Zhang, and R. Bo, "Virtual Inertia Scheduling (VIS) for Real-time Economic Dispatch of IBRs-penetrated Power Systems," *IEEE Trans. Sustain. Energy*, pp. 1–14, 2023.

[3] H. D. Tafti, Q. Wang, C. D. Townsend, J. Pou, and G. Konstantinou, "Global Flexible Power Point Tracking in Photovoltaic Systems Under Partial Shading Conditions," *IEEE Trans. Power Electron.*, vol. 37, no. 9, pp. 11332–11341, Sep. 2022.

[4] K. S. Ratnam, K. Palanisamy, and G. Yang, "Future low-inertia power systems: Requirements, issues, and solutions - A review," *Renew. Sustain. Energy Rev.*, vol. 124, p. 109773, May 2020.

[5] H. Zhang, W. Xiang, W. Lin, and J. Wen, "Grid Forming Converters in Renewable Energy Sources Dominated Power Grid: Control Strategy, Stability, Application, and Challenges," *J. Mod. Power Syst. Clean Energy*, vol. 9, no. 6, pp. 1239–1256, Nov. 2021.

[6] M. Sun, Y. Min, L. Chen, K. Hou, D. Xia, and H. Mao, "Optimal auxiliary frequency control of wind turbine generators and coordination with synchronous generators," *CSEE J. Power Energy Syst.*, vol. 7, no. 1, pp. 78–85, Jan. 2021.

[7] T. Liu, X. Wan, Q. Peng, X. Zeng, Y. Li, and J. Meng, "Dual-mode fast frequency control of PV systems with inertia emulation from DC-link capacitor considering voltage restoration," *CSEE J. Power Energy Syst.*, pp. 1–13, 2024.

[8] L. Wang, Y. Yang, H. Gu, Y. Zhang, C. Wei, and S. Cheng, "Bottleneck Generator Identification and the Corresponding N-1 Frequency Security Constrained Intraday Generator Dispatch," *IEEE Trans. Power Syst.*, vol. 38, no. 1, pp. 739–752, Jan. 2023.

[9] H. Ahmadi and H. Ghasemi, "Security-Constrained Unit Commitment With Linearized System Frequency Limit Constraints," *IEEE Trans. Power Syst.*, vol. 29, no. 4, pp. 1536–1545, Jul. 2014.

[10] Y. Fang, E. Du, H. Jiang, F. Liu, X. Tian, and N. Zhang, "Unit commitment with concentrating solar power considering operational risk and frequency dynamic constraints," *CSEE J. Power Energy Syst.*, pp. 1–13, 2024.

[11] B. Jiang, C. Guo, and Z. Chen, "Frequency constrained unit commitment considering reserve provision of wind power," *Appl. Energy*, vol. 361, p. 122898, May 2024.

[12] Y. Zhang, Q. Guo, Y. Zhou, and H. Sun, "Frequency-constrained unit commitment for power systems with high renewable energy penetration," *Int. J. Electr. Power Energy Syst.*, vol. 153, p. 109274, Nov. 2023.

[13] S. S. Oskouee, S. Kamali, and T. Amraee, "Primary Frequency Support in Unit Commitment Using a Multi-Area Frequency Model With Flywheel Energy Storage," *IEEE Trans. Power Syst.*, vol. 36, no. 6, pp. 5105–5119, Nov. 2021.

[14] D. Wang *et al.*, "Available Inertia Estimation of Induction Machine and Its Effect on Frequency Response of Power Systems with Wind Penetration," in *2019 IEEE Innovative Smart Grid Technologies - Asia (ISGT Asia)*, May 2019, pp. 1783–1787.

[15] L. Wang *et al.*, "Multi-Area Frequency-Constrained Unit Commitment for Power Systems with High Penetration of Renewable Energy Sources and Induction Machine Load," *J. Mod. Power Syst. Clean Energy*, vol. 12, no. 3, pp. 754–766, May 2024.

[16] B. Zhou, R. Jiang, and S. Shen, "Frequency Stability-Constrained Unit Commitment: Tight Approximation Using Bernstein Polynomials," *IEEE Trans. Power Syst.*, pp. 1–13, 2023.

[17] L. Liu, Z. Hu, Y. Wen, and Y. Ma, "Modeling of Frequency Security Constraints and Quantification of Frequency Control Reserve Capacities for Unit Commitment," *IEEE Trans. Power Syst.*, pp. 1–12, 2023.

[18] Z. Zhang, M. Zhou, Z. Wu, S. Liu, Z. Guo, and G. Li, "A Frequency Security Constrained Scheduling Approach Considering Wind Farm Providing Frequency Support and Reserve," *IEEE Trans. Sustain. Energy*, vol. 13, no. 2, pp. 1086–1100, Apr. 2022.

[19] M. Paturet, U. Markovic, S. Delikaraoglou, E. Vrettos, P. Aristidou, and G. Hug, "Stochastic Unit Commitment in Low-Inertia Grids," *IEEE Trans. Power Syst.*, vol. 35, no. 5, pp. 3448–3458, Sep. 2020.

[20] Z. Zhang, E. Du, F. Teng, N. Zhang, and C. Kang, "Modeling Frequency Dynamics in Unit Commitment With a High Share of Renewable Energy," *IEEE Trans. Power Syst.*, vol. 35, no. 6, pp. 4383–4395, Nov. 2020.

[21] A. Dixon, *Modern Aspects of Power System Frequency Stability and Control*. Academic Press, 2019.

[22] Y. Shen, W. Wu, B. Wang, and S. Sun, "Optimal Allocation of Virtual Inertia and Droop Control for Renewable Energy in Stochastic Look-Ahead Power Dispatch," *IEEE Trans. Sustain. Energy*, vol. 14, no. 3, pp. 1881–1894, Jul. 2023.

[23] V. Knap, S. K. Chaudhary, D.-I. Stroe, M. Swierczynski, B.-I. Craciun, and R. Teodorescu, "Sizing of an Energy Storage System for Grid Inertial Response and Primary Frequency Reserve," *IEEE Trans. Power Syst.*, vol. 31, no. 5, pp. 3447–3456, Sep. 2016.

[24] H. Golpîra, A. Atarodi, S. Amini, A. R. Messina, B. Francois, and H. Bevrani, "Optimal Energy Storage System-Based Virtual Inertia Placement: A Frequency Stability Point of View," *IEEE Trans. Power Syst.*, vol. 35, no. 6, pp. 4824–4835, Nov. 2020.

[25] L. Badesa, F. Teng, and G. Strbac, "Simultaneous Scheduling of Multiple Frequency Services in Stochastic Unit Commitment," *IEEE Trans. Power Syst.*, vol. 34, no. 5, pp. 3858–3868, Sep. 2019.

[26] G. Zhang, E. Ela, and Q. Wang, "Market Scheduling and Pricing for Primary and Secondary Frequency Reserve," *IEEE Trans. Power Syst.*, vol. 34, no. 4, pp. 2914–2924, Jul. 2019.

[27]P. Kundur, *Power System Stability and Control*, New York, NY, USA: McGraw-Hill, 1994.
[28]J. Li, Y. Qiao, Z. Lu, W. Ma, X. Cao, and R. Sun, "Integrated Frequency-Constrained Scheduling Considering Coordination of Frequency Regulation Capabilities from Multi-Source Converters," *J. Mod. Power Syst. Clean Energy*, pp. 1–14, 2023.
[29]M. Javadi, Y. Gong, and C. Y. Chung, "Frequency Stability Constrained BESS Sizing Model for Microgrids," *IEEE Trans. Power Syst.*, pp. 1–13, 2023.
[30]K. Antoniadou-Plytaria, D. Steen, L. A. Tuan, O. Carlson, B. Mohandes, and M. A. F. Ghazvini, "Scenario-Based Stochastic Optimization for Energy and Flexibility Dispatch of a Microgrid," *IEEE Trans. Smart Grid*, vol. 13, no. 5, pp. 3328–3341, Sep. 2022.
[31]T. Ding, Z. Zeng, M. Qu, J. P. S. Catalão, and M. Shahidehpour, "Two-Stage Chance-Constrained Stochastic Thermal Unit Commitment for Optimal Provision of Virtual Inertia in Wind-Storage Systems," *IEEE Trans. Power Syst.*, vol. 36, no. 4, pp. 3520–3530, Jul. 2021.
[32]Y. Zhang, S. Wu, J. Lin, Q. Wu, C. Shen, and F. Liu, "Frequency Reserve Allocation of Large-Scale RES Considering Decision-Dependent Uncertainties," *IEEE Trans. Sustain. Energy*, pp. 1–15, 2023.
[33]U. Markovic, Z. Chu, P. Aristidou, and G. Hug, "LQR-Based Adaptive Virtual Synchronous Machine for Power Systems With High Inverter Penetration," *IEEE Trans. Sustain. Energy*, vol. 10, no. 3, pp. 1501–1512, Jul. 2019.
[34]Q. Shi, F. Li, and H. Cui, "Analytical Method to Aggregate Multi-Machine SFR Model With Applications in Power System Dynamic Studies," *IEEE Trans. Power Syst.*, vol. 33, no. 6, pp. 6355–6367, Nov. 2018.
[35]C. Wang, R. Zhang, and T. Bi, "Energy Management of Distribution-Level Integrated Electric-Gas Systems With Fast Frequency Reserve," *IEEE Trans. Power Syst.*, pp. 1–15, 2023.
[36]B. Zhou *et al.*, "Partial-Dimensional Correlation-Aided Convex-Hull Uncertainty Set for Robust Unit Commitment," *IEEE Trans. Power Syst.*, vol. 38, no. 3, pp. 2434–2446, May 2023.
[37]G. Huang, J. Wang, C. Chen, J. Qi, and C. Guo, "Integration of Preventive and Emergency Responses for Power Grid Resilience Enhancement," IEEE Trans. Power Syst., vol. 32, no. 6, pp. 4451–4463, Nov. 2017.
[38]C. Shao, X. Wang, M. Shahidehpour, X. Wang, and B. Wang, "Security-Constrained Unit Commitment With Flexible Uncertainty Set for Variable Wind Power," *IEEE Trans. Sustain. Energy*, vol. 8, no. 3, pp. 1237–1246, Jul. 2017.
[39]P. M. Anderson and M. Mirheydar, "A low-order system frequency response model," *IEEE Trans. Power Syst.*, vol. 5, no. 3, pp. 720–729, Aug. 1990.
[40]F. Li and R. Bo, "DCOPF-Based LMP Simulation: Algorithm, Comparison With ACOPF, and Sensitivity," *IEEE Trans. Power Syst.*, vol. 22, no. 4, pp. 1475–1485, Nov. 2007.
[41]Illinois Institute Of Illinois Institute Of Technology Electrical And Computer Engineering Database [Online]. Available: http://motor.ece.iit.edu/data/